Materials Advances

ROYAL SOCIETY OF CHEMISTRY

PAPER

View Article Online
View Journal | View Issue

Cite this: *Mater. Adv.*, 2024, 5, 5070

Mechanochemical effect on the electrochemical properties of a $Na_3(VO)_2(PO_4)_2F$ positive electrode for sodium-ion batteries†

William G. Morais, *‡ Eduardo C Melo and Roberto M. Torresi *

Sodium vanadium fluorophosphate (NVPF) has shown promising properties as a positive electrode in sodium-ion batteries mainly due to its high operating voltage; however, it has significant electronic and kinetic limitations that must be addressed. In this study, we investigated how a simple and straightforward mechanochemical treatment can be a valuable alternative to overcome these limitations. NVPF electrodes before and after (NVPF-bm) mechanochemical treatment were compared. For NVPF-bm, the contribution from the sodiation/desodiation of Na_1^+ increased from 23 to 40% as Na_2^+ decreased from 38 to 48% of the total produced capacity at ~0.5 C (70 mA g^{-1}); additionally, the discharge capacities were 30% greater than those of NVPF at 0.8 C (100 mA g^{-1}); nevertheless, after 150 cycles, NVPF-bm presented a coulombic efficiency of 96.2% and a capacity retention of 82.6%. The calculated diffusion coefficients for NVPF-bm were 22 × 10^{-10} and 1.0 × 10^{-10} cm^2 s^{-1}, compared to 6.5 × 10^{-11} and 2.5 × 10^{-11} cm^2 s^{-1} for NVPF for the sodiation and desodiation processes, respectively. Furthermore, for the charge and discharge processes, NVPF-bm presented a charge transfer resistance three times smaller and diffusion lengths of 2.1 and 0.3 μm, respectively, compared to 8.0 and 13 μm, respectively, for NVPF. These results demonstrate the kinetic enhancements of the electrode as a direct consequence of the mechanochemical treatment. Therefore, this approach impacts not only the synthesis and morphology but also the inherent electrochemical storage capacity of the NVPF.

Received 2nd February 2024,
Accepted 27th April 2024

DOI: 10.1039/d4ma00106k

rsc.li/materials-advances

1. Introduction

The technological transition from fossil fuel dependence toward renewable sources remains a challenge for the energy research community. To increase the efficiency of this transition, low-cost, safe and environmentally friendly batteries are needed. Lithium-ion batteries (LIBs) remain the top choice for commercial application due to their excellent specific energy of 250–300 W h kg^{-1}; however, they present relevant disadvantages that arise from metal availability and cost, creating tensions regarding critical raw materials and, consequently, compromising their application in large-scale systems.[1,2]

Sodium-ion batteries (SIBs) have been demonstrated to be viable alternatives, especially for large-scale devices, owing to the abundance and wide distribution of sodium, cost-effectiveness (*i.e.*, aluminum as a current collector), and fundamental principles similar to those of LIBs, which have resulted in the exponential progression of SIB studies over the last few years. Furthermore, the overall cost of the extraction and purification of Na grants SIBs approximately 20–30% lower production costs than those of LIBs.[3–5] Nevertheless, sodium ions are larger and heavier (1.02 Å and 22.99 g mol^{-1}) than lithium ions (0.76 Å and 6.94 g mol^{-1}), affecting the energy density of the SIB (90–160 W h kg^{-1}).[6,7]

Regarding the materials investigated as positive electrodes, sodium vanadium fluorophosphate (NVPF), chemically defined as $Na_3V_2(PO_4)_2O_{2x}F_{3-2x}$, has gained extensive attention due to its remarkably high working potential (~4.1 V), which arises from the inductive effect of PO_4^{3-} coupled with F^- anions combined with a NASICON-type structure that provides three-dimensional frameworks with large interstitial channels and a theoretical capacity of ~130 mA h g^{-1}.[8–10] However, NVPF suffers from poor electronic conductivity and kinetic limitations, which restrict its performance at high current densities. Among the strategies used to overcome these problems, surface modification with conductive carbon materials, nanoscale architecture and doping with heteroatoms have been proven to promote positive results.[11–14]

Departamento de Química Fundamental, Instituto de Química, Universidade de São Paulo, Av. Prof. Lineu Prestes, 748, 05508-000, São Paulo, SP, Brazil.
E-mail: wgomesdemorais@fbk.eu, rtorresi@iq.usp.br

† Electronic supplementary information (ESI) available: XPS spectra and corresponding deconvolution; fitting of the d*Q*/d*E* peaks of the electrodes; capacity contribution of Na_1^+ and Na_2^+; post-mortem SEM images; cyclic voltammograms. See DOI: https://doi.org/10.1039/d4ma00106k

‡ Present address: Center for Sustainable Energy – SE, Fondazione Bruno Kessler – FBK. *Via* Sommarive 18, 38123 Povo (TN), Italy.

The use of mechanochemistry is eco-friendly because it allows for material synthesis and/or structural modifications without the use of organic-based solvents or high sintering temperatures.[15–17] This method, when used posttreatment in as-synthesized electroactive materials, can provide good electrochemical responses for both sensors and energy storage applications as long as it does not lead to amorphization.[18–20] Studies have been conducted on fluorophosphate-based positive electrodes for SIBs, focusing on the synthesis benefits of mechanochemical treatment,[21,22] but the specific effect on the electrochemical storage properties has not been properly addressed until now.

In our study, we uncover the mechanisms driving the improvement of NVPF electrode performance, especially pronounced under high current densities, *via* a simple and rapidly controlled posttreatment mechanochemical process. Our research contributes a significant novelty as we explore this avenue. By analyzing calculated diffusion coefficients and electrochemical impedance, we validate the heightened ionic mobility and improved electronic and kinetic properties implicated in the intercalation and deintercalation processes along 150 cycles. This advancement lies in the reduction of Na^+ diffusion pathways while maintaining the integrity of the crystal structure.

2. Experimental section

2.1. Material preparation

NVPF was synthesized at low temperature by following our previously reported synthetic route.[11] A mixture of the precursors V_2O_5 (Sigma-Aldrich) and $C_2H_2O_4$ (Synth) was prepared in 70 mL of H_2O at 60 °C with magnetic stirring for 2 h. After that, a blue solution was obtained as vanadium was reduced by oxalic acid and formed the VOC_2O_2 intermediate. Then, the precursors NaF (Sigma-Aldrich), Na_2SO_4 (Synth) and Na_2HPO_4 (Synth) were added at a molar ratio of 1 : 2 : 1 : 3, and the solution was stirred in a hermetic container for 20 h at 100 °C. The obtained precipitate was filtered and dried at 120 °C. Finally, the mechanochemical treatment was carried out with the aid of an SL-38 Solab ball mill in a Teflon jar using three zirconia milling balls (15 mm and 3.15 g each) for 30 minutes to obtain NVPF-bm.

2.2. Structural analysis

Powder X-ray diffraction analysis was used to characterize the NVPF and NVPF-bm crystallographic structures and phases with the aid of a Phillips Empyrean diffractometer with a Cu Kα radiation source generated at 45 kV and 40 mA in a 2θ range of 10–60°. The morphology of the samples was studied by scanning electron microscopy (SEM) with the aid of a JEOL JSM-7401F instrument. Post-mortem SEM images were obtained using a JEOL Neoscope JCM-5000. Brunauer–Emmett–Teller (BET) method was used to obtain the surface area and non-local density functional theory (NLDFT) model was used to determine the pore size distribution of the materials. For this purpose, the samples were degassed at 120 °C overnight prior to analysis, which was carried out at 77 K using N_2 as the absorbate in Quantachrome 1000e surface analyzer. The X-ray photoelectron spectra (XPS) were obtained with a SPECSLAB II (Phoibos-Hsa 3500 150, 9 channeltrons) spectrometer with Al Kα radiation, which provide photons at 1486.6 eV in the Brazilian Synchrotron Light Laboratory (LNLS, Campinas, SP, Brazil), operating at 12 kV, a pass energy (Epass) of 40 eV, an energy step of 0.1 eV and an acquisition time of 1 s per point; the internal residual pressure was approximately 1×10^{-8} Torr. All XPS data were referenced according to the adventitious C 1 s peak (284.5 eV).

2.3. Electrochemical analysis

The NVPF and NVPF-bm electrodes were prepared by mixing the active material with carbon black (Timical Super P C65, MTI) and the binder polyvinylidene fluoride (PVDF, MTI) at a mass ratio of 80 : 10 : 10 using *N*-methyl-2-pyrrolidone (NMP, Sigma-Aldrich) as a solvent to form a homogenous slurry. The prepared slurry was used to coat Al foils using a doctor blade technique (150 μm thickness), after which it was dried at 120 °C under vacuum overnight and then cut into disks with diameters of 10 and 12 mm and a mass loading of 2 mg cm^{-2}. CR2016-type coin cells were assembled with the obtained fluorophosphates and a sodium disk as positive and negative electrodes, respectively. Additionally, three-electrode Swagelok cells were prepared using the samples as the working electrode and sodium disks as the counter and quasireference electrodes, respectively. Both the coin and Swagelok cells were assembled in an Ar-filled glove box with 1 M $NaClO_4$ in EC/PC (50 : 50) as the electrolyte and glass fiber (Whatman, GF/F) as the separator. Cyclic voltammetry (CV) and electrochemical impedance spectroscopy (EIS) were performed with Swagelok cells by an Autolab M101 potentiostat/galvanostat (Metrohm), while coin cells were used for the galvanostatic intermittent titration technique (GITT) and battery tests, which were carried out with a Biologic BCS 805 battery tester.

3. Results and discussion

Fig. 1a shows the XRD patterns of the NVPF and NVPF-bm powder samples. These diffraction peaks correspond to tetragonal NVPF (JCPDS No: 96-153-5057) and are indexed in tetragonal symmetry with *I*4/*mmm*.[23] The three-dimensional framework of these fluorophosphates consists of $[V_2O_{10}F]$ bioctahedra formed by two VO_5F octahedra with a corner-sharing F in the *c*-axis direction, which are bridged with $[PO_4]$ tetrahedra by shared O atoms to form a pseudolayered structure. The reversible intercalation/deintercalation of sodium ions is possible due to two interstitial sites formed in the *b*- and *c*-axis directions, Na_1^+ and Na_2^+, respectively.[11,24] Additionally, the NVPF-bm diffraction peaks are slightly shifted to higher 2θ values, suggesting that a greater cell volume is obtained *via* mechanochemistry; nevertheless, these results confirm that the crystal structure of NVPF-bm is preserved after posttreatment.[25]

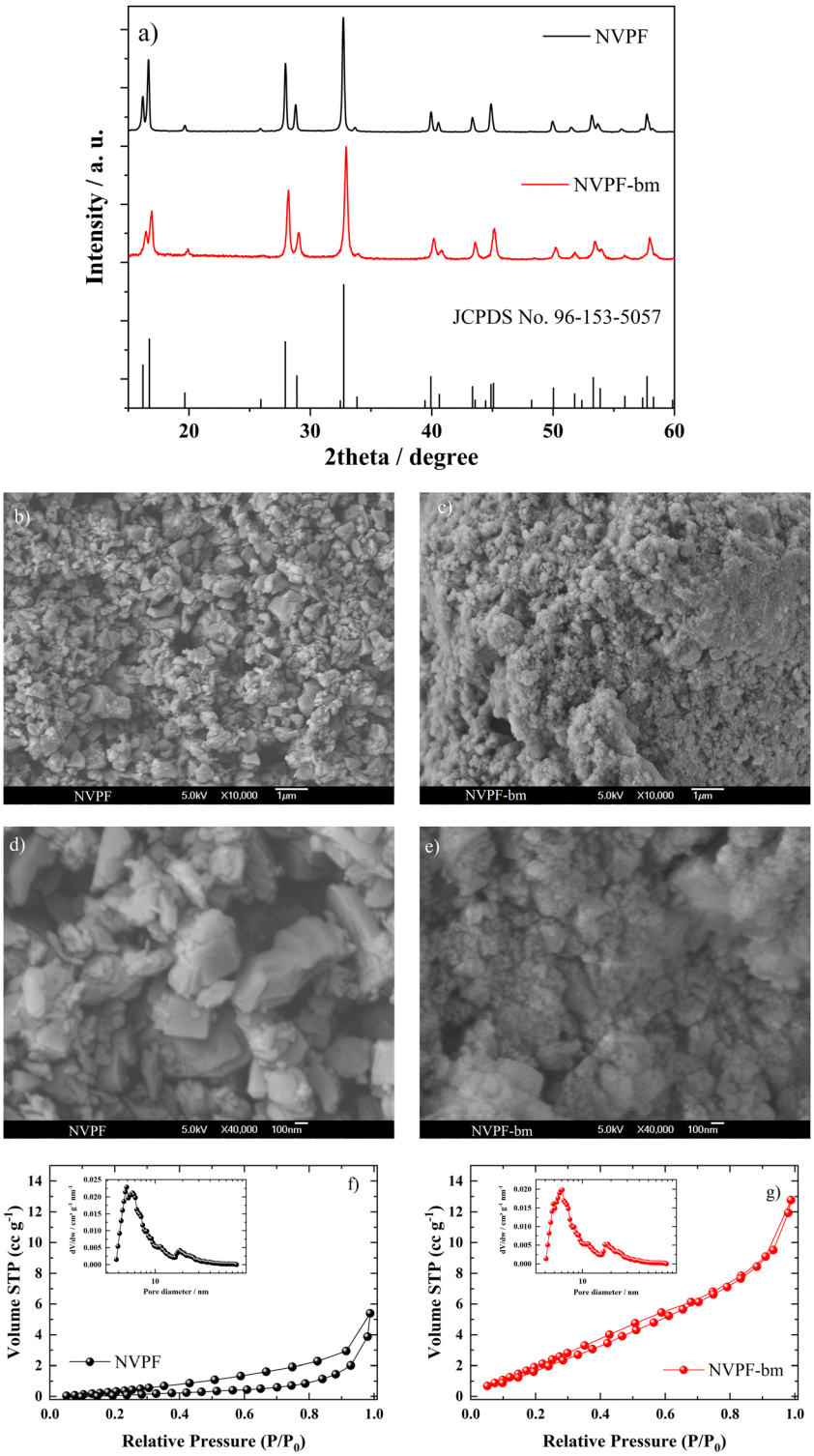

Fig. 1 (a) XRD patterns of the NVPF and NVPF-bm samples and a standard comparison card. SEM images of (b) and (d) NVPF and (c) and (e) NVPF-bm. Nitrogen adsorption/desorption curves of (f) NVPF and (g) NVPF-bm electrodes. Inset: Pore-size distribution.

The morphological characteristics of the samples were evaluated with the aid of SEM images (Fig. 1b–e). A comparison of the NVPF before and after treatment in Fig. 1b and d, and Fig. 1c and e, respectively, shows that NVPF-bm has a grainier surface, forming agglomerates with diameters of 300–400 nm, while NVPF has agglomerates with diameters of 600–700 nm. The mechanochemical treatment clearly promoted a comminution effect on the particle agglomerates, reducing the grain size, which might positively impact the ionic mobility inside the fluorophosphate when used as an electrode.

The BET surface area and pore size distribution of the materials are investigated by nitrogen isothermal adsorption measurement as depicted in Fig. 1f and g. Both samples exhibit an IV-type isotherm, indicating mesoporous characteristics. The pore size distribution curves are provided in Fig. 1f and g, revealing similar average pore size of NVPF (20.9 nm) and NVPF-bm (21.4 nm). Additionally, NVPF-bm demonstrates a higher surface area of 87 $m^2\ g^{-1}$ compared to 18.5 $m^2\ g^{-1}$ of NVPF, suggesting the presence of more pores and adsorption sites conducive to efficient electrolyte infiltration.

The chemical composition and oxidation states of NVPF and NVPF-bm were investigated *via* XPS analysis. The wide spectra of the electrodes are shown in Fig. 2a, while the spectra of vanadium, sodium and oxygen are shown in Fig. 2b and Fig. S1a, S1b (ESI†), respectively. The two intense peaks located at 522.9 and 516.7 eV are attributed to V $2P_{3/2}$ and V $2p_{1/2}$, respectively, relative to the split of the V 2p peak attributed to V^{4+} species. Additionally, a weak peak is observed at 520.3 eV, which can be attributed to low amounts of V^{3+} in the NVPF.[22,26] These results confirmed that the mechanochemical treatment did not modify the chemical properties of the materials prior to their use as electrodes.

The galvanostatic charge and discharge curves for NVPF and NVPF-bm are shown in Fig. 3a and b, respectively. The NVPF electrode had capacities of 64.9, 47.0, 24.8 and 17.9 mA h g^{-1}, while NVPF-bm had capacities of 53.4, 50.6, 45.2 and 41.9 mA h g^{-1} at current densities of 0.01, 0.02, 0.05 and 0.07 A g^{-1}, respectively. At high current densities, NVPF-bm exhibited better performance than NVPF, which raised the possibility of higher ionic mobility inside the material being obtained by mechanochemical posttreatment; thus, we decided to further investigate the storage properties of the electrodes by determining the first derivative of the galvanostatic curves.

Fig. 3c and d show the differential capacity (dQ/dE) plots of NVPF and NVPF-bm, respectively. Two peaks are observed, both due to the V^{IV}/V^{V} redox couple and related to two types of sodium ions and two sodiation/desodiation mechanisms. The reaction at 3.63/3.60 V is associated with Na^+ type 1 (Na^+_1) and occurs *via* a two-phase reaction, while the reaction at 4.01/3.99 V is related to Na^+ type 2 (Na^+_2) and occurs *via* a solid solution.[27,28]

Based on the dQ/dE plots, it was possible to separate the contributions from each type of Na^+ to the produced capacities by fitting the redox peaks (see Fig. S2 and S3, ESI†). Fig. 4 shows the percent contributions of both Na^+_1 and Na^+_2 to the charge/discharge processes of the (a and b) NVPF and (c and d) NVPF-bm electrodes. Another approach can be found in Fig. S4 (ESI†), where the contributions of each type of Na^+ are plotted separately. When the NVPF electrode is charged, the contribution of Na^+_1 changes from 50 to 23%, while for the discharge process, the contribution changes from 34 to 62% as the applied current increases from 10 to 70 mA g^{-1}. These results indicate sluggish kinetics for both Na^+_1 and Na^+_2 during desodiation and sodiation, respectively.

In the case of NVPF-bm, both Na^+_1 and Na^+_2 provided more equivalent contributions to the capacities; additionally, it was noted that the capacity contribution from Na^+_1 changed from 52 to 40% during charging and from 57 to 52% during discharging as the applied current shifted from 10 to 70 mA g^{-1}. Based on these results, it can be assumed that the kinetics of both desodiation of Na^+_1 and sodiation of Na^+_2 were mechanochemically improved. To verify this hypothesis, new evidence was obtained *via* kinetic measurements and will be further discussed.

The rate capability of the electrodes at the same voltage window of the previous galvanostatic curves can be seen in Fig. 5a. NVPF produced higher capacities at low current densities but failed to maintain this performance when the applied current increased, with the capacities dropping 30% per applied current, while for NVPF-bm, the produced capacities decreased 15% per applied current; however, at high currents, the performance was far superior. NVPF-bm presenting smaller capacities at low currents is related to the low electronic conductivity of the polyanion, which seems to be less affected than the posttreatment ionic conductivity. To compensate for this effect, longer charging is needed.

Fig. 5b shows the rate capability of the electrodes with a broad voltage window of 1–4.5 V. Under these conditions, NVPF-bm exhibited more stable behavior at different current ranges with a discharge capacity equivalent to that of the NVPF electrode, 100 mA h g^{-1} at 10 mA g^{-1}. Additionally, the NVPF-bm electrode exhibited remarkable charge reversibility over a wide potential window, with capacities of 95.9 and 91.9 mA h g^{-1}

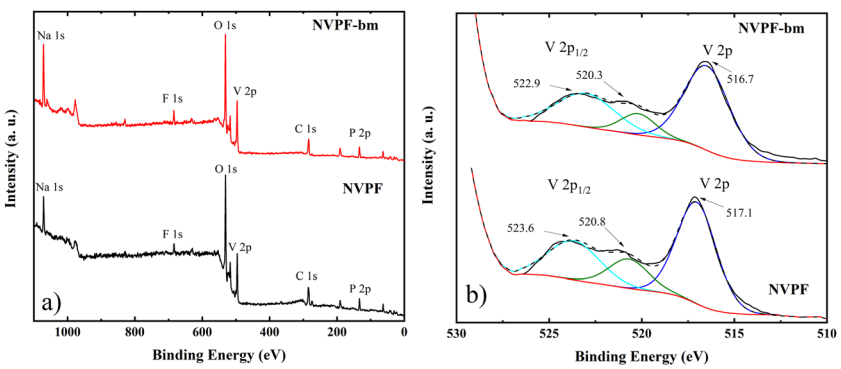

Fig. 2 (a) Wide-scan XPS spectra and corresponding deconvolution results of the orbital peak; (b) V 2p of the NVPF and NVPF-bm electrodes.

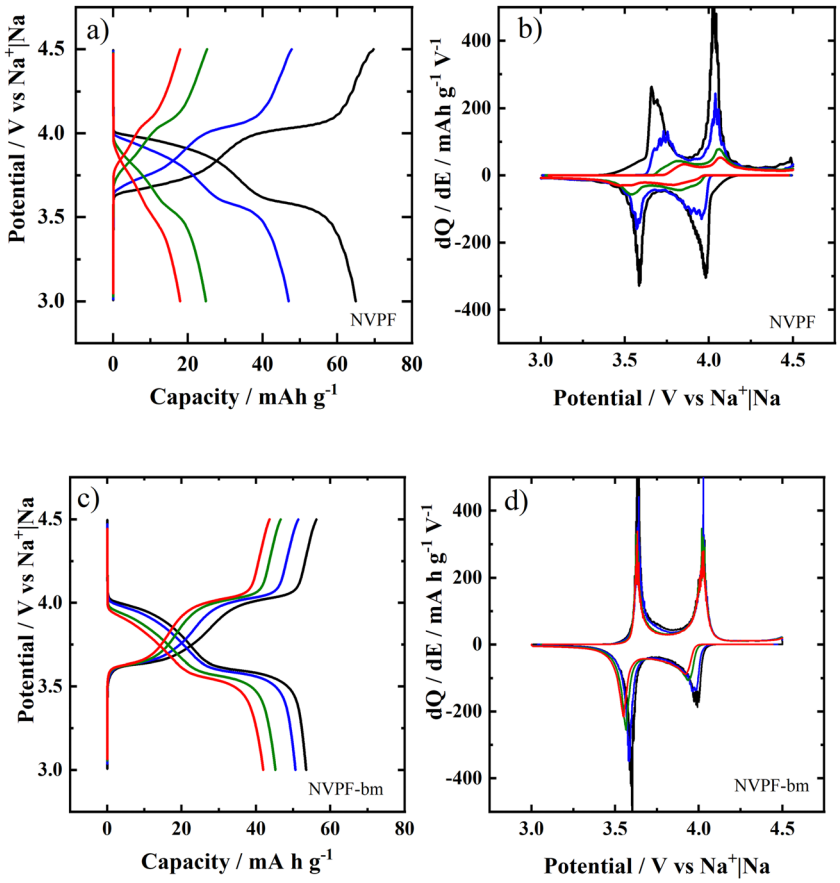

Fig. 3 Charge and discharge curves (10th cycle) and dQ/dE plots as a function of the potential of the NVPF (a) and (b) and NVPF-bm (c) and (d) electrodes at 0.01 (—), 0.02 (–), 0.05 (–) and 0.07 (–) A g^{-1}.

for the 10th and 100th cycles of charge/discharge, respectively (Fig. S5a and b, ESI†).

The results of the cycling tests of the NVPF and NVPF-bm electrodes are shown in Fig. 5c, in which the charge and discharge capacities and the coulombic efficiency as a function of the number of cycles are shown. The curves of the 1st, 50th, 100th and 150th cycles are shown in Fig. S5c and d (ESI†). NVPF-bm exhibited discharge capacities of 54.5, 51.1 and 47.3 mA h g for the 50th, 100th and 150th cycles, respectively, with a coulombic efficiency of 96.2% and a capacity retention of 82.6% from the 20th to 150th cycles, while the NVPF electrode exhibited discharge capacities of 45.9, 44.5 and 43.7 mA h g^{-1} for the 50th, 100th and 150th cycles, respectively, with a coulombic efficiency of 98.7% and a capacity retention of 91.2%. Additionally, the initial Coulombic efficiency slightly improved from 48.3 to 52.4% for the NVPF and NVPF-bm electrodes, respectively. Moreover, the NVPF-bm electrode exhibited no evident cracking and smaller particle agglomerates compared to the NVPF electrode, even after experiencing severe electrolyte decomposition, as evidenced by the post-mortem SEM images (Fig. S6a, b and S6c, d, respectively, ESI†).

The cyclic voltammograms of NVPF and NVPF-bm are shown in Fig. S7(a and c) (ESI†), respectively, and two pairs of redox peaks were identified at ~3.7 V (R1–O1) and ~4.1 V (R2–O2). As discussed before, the R1–O1 pair is related to the intercalation/deintercalation of Na^{+}_{1} by a two-phase reaction mechanism, while R2–O2 is associated with a solid-solution reaction mechanism involving Na^{+}_{2}.[27] Compared to the NVPF voltammograms, the NVPF-bm electrode shows well-defined redox peaks for all scan rates, which indicates equivalent accessibility to the active sites through both intercalation mechanisms, demonstrating the increase in kinetics due to the mechanochemical treatment, which agrees with the galvanostatic results. Additionally, it is possible to observe that NVPF-bm presented a more reversible behavior when comparing the amount of charge that intercalated and deintercalated the electrode at different scan rates (Fig. S7b and d, ESI†).

The mobility of electroactive species inside the electrode is a key parameter that affects both the performance and longevity of the cell. For this purpose, the GITT technique was used to estimate Na^{+} diffusion, which consisted of applying current pulses (0.02 A g^{-1} for 600 s) and a relaxation time of 60 min to reach electrochemical equilibrium. Assuming specific boundary conditions, Fick's second law of diffusion can be used to obtain eqn (1).[29–31]

$$D_s = \frac{4}{\pi}\left(\frac{V_m}{FSz_i}\right)^2\left[I_0\left(\frac{dE}{d\delta}\right)\Big/\left(\frac{dE}{d\sqrt{\tau}}\right)\right]^2\left(\tau \ll \frac{L^2}{D_{Na}}\right) \quad (1)$$

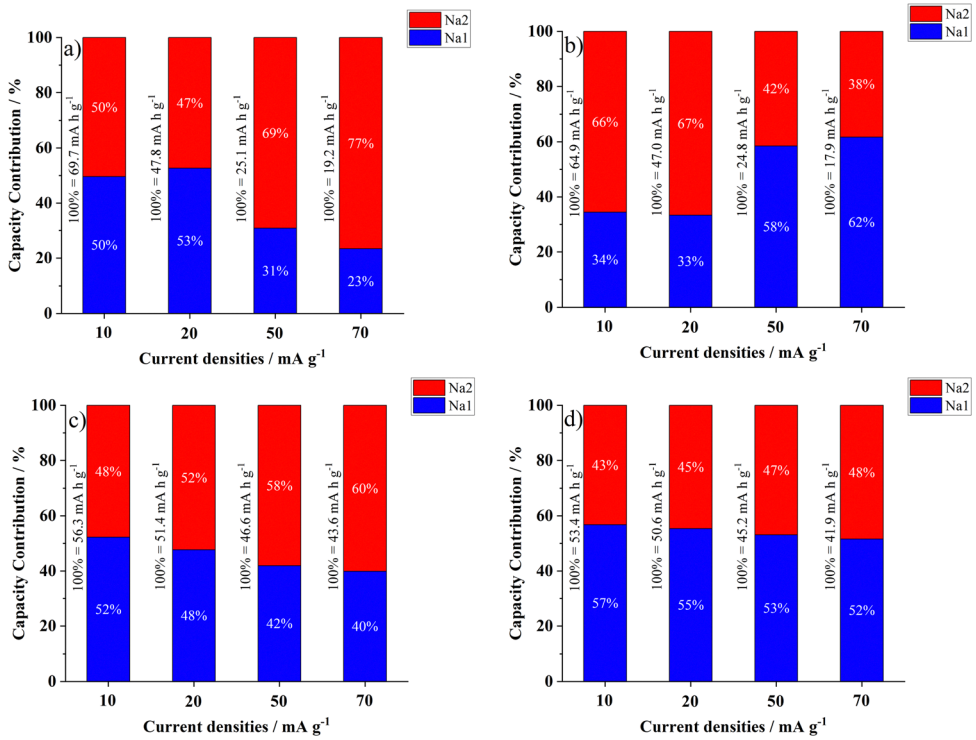

Fig. 4 Capacity contributions of (blue) $Na^{+}{}_1$ and (red) $Na^{+}{}_2$ to the (a) and (c) charge and (b) and (d) discharge processes of the (a) and (b) NVPF and (c) and (d) NVPF-bm electrodes.

where D_{Na} is the sodium chemical diffusion coefficient ($cm^2\ s^{-1}$), τ represents the duration of the current pulse (600 s), S refers to the area of the electrode (1.13 cm^2), V_m is the molar volume of the active material and L is the length of the diffusion path (cm). Eqn (1) can be further simplified when sufficiently small current pulses are applied for short time intervals; in this case, the $\frac{dE}{d\sqrt{t}}$ ratio can be considered linear, and the coulometric titration curve can be assumed to be linear over the composition range, which yields:

$$D_{Na} = \frac{4}{\pi\tau}\left(\frac{n_m V_m}{S}\right)^2\left(\frac{\Delta E_s}{\Delta E_\tau}\right)^2 \quad (2)$$

where ΔE_S represents the steady-state voltage change due to the current pulse, and ΔE_τ is the voltage change during the constant current pulse.

Fig. 6(a–d) shows the variations in the sodium diffusion coefficient, molar fraction, and dQ/dE as a function of the cell potential of the fluorophosphate electrodes. In general, the D_{Na} of NVPF-bm reached $\sim 10^{-9}\ cm^2\ s^{-1}$, while that of NVPF ranged from $\sim 10^{-12}$ to $10^{-10}\ cm^2\ s^{-1}$. For both the charge and discharge processes, the D_{Na} values associated with the $Na^{+}{}_1$ intercalation mechanism are close to 3.0×10^{-13} and $7.5 \times 10^{-11}\ cm^2\ s^{-1}$ for the NVPF and NVPF-bm electrodes, respectively, while for $Na^{+}{}_2$, the obtained values are in the range of 4.5×10^{-11} and $2.0 \times 10^{-10}\ cm^2\ s^{-1}$ for NVPF and NVPF-bm, respectively. These results suggest that the average distance of the diffusion paths in NVPF-bm is markedly reduced compared to that in NVPF, which facilitates ionic mobility inside the host material. Moreover, the two-phase reaction kinetic, related to $Na^{+}{}_1$ intercalation/deintercalation, has been improved as a direct effect of mechanochemical treatment.

The EIS results for both the NVPF and NVPF-bm electrodes after 10 cycles of charge and discharge are shown in Fig. 7(a and b) as Nyquist and Bode plots, respectively, and the electrochemical equivalent circuit used to represent the system is shown in Fig. 7c. A small semicircle related to the CEI layer is identified at high frequencies, while another semicircle is found at intermediate frequencies associated with charge transfer; at low frequencies, a straight line due to diffusion of the species is observed.[32]

To obtain the kinetic parameters, the experimental EIS data were adjusted through the equivalent circuit shown in Fig. 7c. In this circuit, R_s, R_{cei} and R_{ct} are the resistance of the solution, the CEI and the charge transfer, respectively, while the constant phase elements are represented by CPE_1 and CPE_2. The effective capacitance values C_{cei} and C_{dl} are obtained with the aid of eqn (3) and are related to the CEI and double layer, respectively.[33] The diffusion of the species is represented by the Warburg impedance (W).

$$C_{eff} = \left[Q\left(\frac{1}{R_1} + \frac{1}{R_2}\right)^{(n-1)}\right]^{\frac{1}{n}} \quad (3)$$

The parameters obtained through the fitting process are shown in Table 1. Compared to those of NVPF, the R_{ct} values of NVPF-bm were three times smaller, in agreement with the almost imperceptible second semicircle in Fig. 7b, indicating an increase in the electronic conductivity of the material.

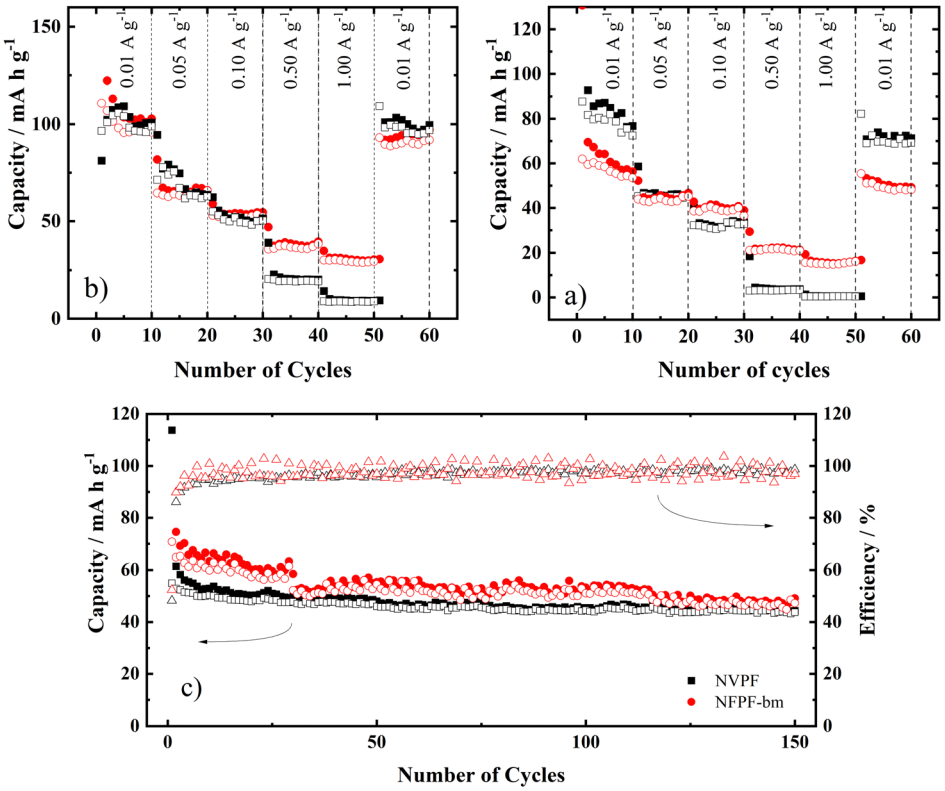

Fig. 5 Rate capability of the NVPF (■ charge, □ discharge) and NVPF-bm (● charge, ○ discharge) electrodes at (a) 3–4.5 and (b) 1–4.5 V. Samples were charged at 0.01 A g^{-1} and discharged at 0.01, 0.05, 0.10, 0.50 and 1.00 A g^{-1}. (c) Cyclability of NVPF (■ charge, □ discharge, Δ efficiency) and NVPF-bm (● charge, ○ discharge, △ efficiency) charged at 0.01 and discharged at 0.02 A g^{-1}.

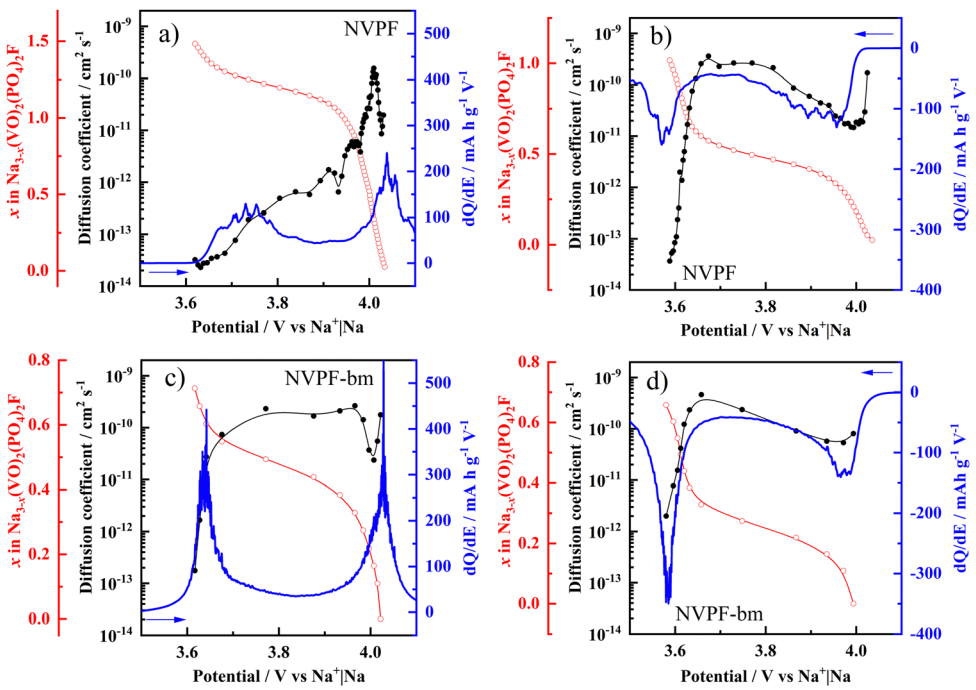

Fig. 6 Sodium diffusion coefficient (---), molar fraction (–○–), and dQ/dE (— —) as a function of the cell potential of the charge and discharge processes for the NVPF (a) and (b) and NVPF-bm (c) and (d) electrodes. Charging and discharging occurred at 0.02 A g^{-1}.

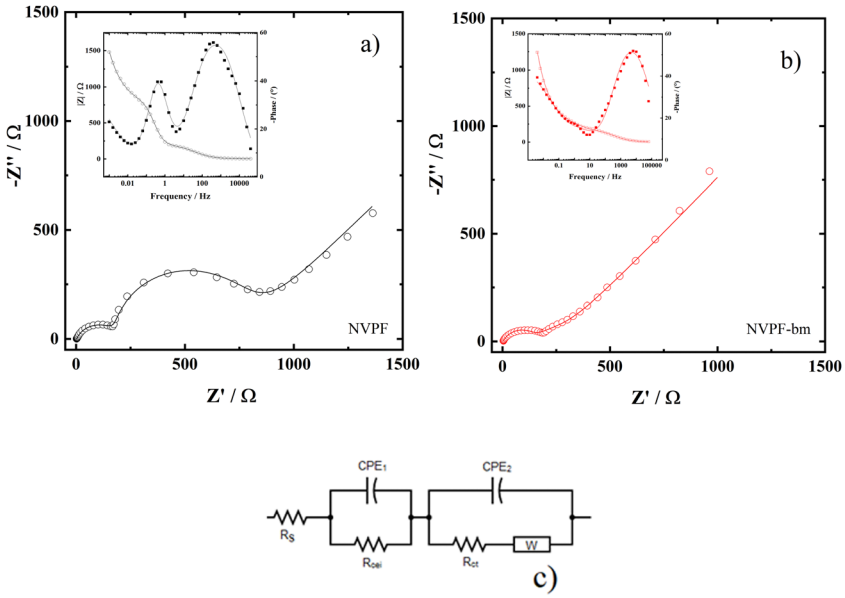

Fig. 7 EIS Nyquist (○) diagrams and (—) fitting of (a) NVPF and (b) NVPF-bm. (c) Equivalent electric circuit used to fit the impedance data. Inset: Bode plots.

Table 1 Obtained parameters of the EIS fitting data

	NVPF	NVPF-bm
E/V	3.60	3.68
R_s/Ω	2.4 ± 0.8	2.8 ± 0.3
R_{cei}/Ω	184 ± 5	147 ± 20
C_{cei}/μF	6.3 ± 0.5	0.7 ± 0.1
R_{ct}/Ω	584 ± 2	196 ± 36
C_{dl}/mF	1.28 ± 0.8	0.04 ± 0.01
x	1	1
Area (electrode)/cm^2	0.79	0.79
Mass (electrode)/mg	0.97	0.94

A smaller R_{CEI} is also observed for NVPF-bm related to the CEI layer, which acts as a protective layer on the electrode.[34–36] These results agree with what was observed by CV and GITT measurements, indicating that mechanochemical treatment promoted enhancements in both ionic and electronic kinetics.

Furthermore, the EIS data were coupled with the GITT results to estimate the diffusion length l_D of the electrodes with the aid of eqn (4):

$$l_D = \sqrt{\tau_D . D} \quad (4)$$

in which D is the diffusion coefficient, and τ_D is the characteristic diffusion time constant. When one assumes that the concentration gradients of charge transfer at the interface and within the solid are equal, τ_D can be replaced by τ_s, a lifetime constant that is computed by extending the frequency range to 10^{-3} Hz for the fitted equivalent circuit of the EIS (2.5 s for the NVPF and 0.4 s for the NVPF-bm).[37] Based on the GITT results, the average diffusion coefficients for NVPF are 2.5×10^{-11} and 6.5×10^{-11} cm^2 s^{-1}, and for NVPF-bm, they are 1.0×10^{-10} and 22×10^{-10} cm^2 s^{-1} for the charge and discharge processes, respectively. Therefore, the obtained l_D values were 8.0 and 13 μm for NVPF and 2.1 and 0.3 μm for NVPF-bm for the charge and discharge processes, respectively. These results provide additional evidence of mechanochemical enhancement as the diffusion paths decreased during both the sodiation and desodiation reactions.

4. Conclusion

Sodium vanadium fluorophosphate-based electrodes without (NVPF) and with (NVPF-bm) a mechanochemical posttreatment were obtained and compared as positive electrodes for SIBs. The crystal structure of NVPF-bm was not only preserved but also enlarged, as seen in the XRD patterns, while morphological analysis revealed a comminution effect that reduced the size of the agglomerates of particles. With the aid of the galvanostatic curves and differential capacity plots, it was possible to separately analyze the capacity contributions of both types of Na^+ during the charge/discharge processes. At 70 mA g^{-1}, the contribution of Na^+_1 increased from 23 to 40%, while that of Na^+_2 changed from 38 to 48% of the produced capacity after the treatment, suggesting that the kinetic of both the desodiation of Na^+_1 and the sodiation of Na^+_2 were mechanochemically improved. The rate capacity performance was significantly enhanced by posttreatment, with NVPF-bm producing discharge capacities greater than 30% greater than those of NVPF at 0.1 A g^{-1}; after 150 cycles, it presented a capacity retention of 82.6% with a coulombic efficiency of 96.2%. Ionic mobility was investigated with the aid of GITT. The average diffusion coefficients of NVPF-bm were 22×10^{-10} and 1.0×10^{-10} cm^2 s^{-1}, while those of NVPF were 6.5×10^{-11} and 2.5×10^{-11} cm^2 s^{-1} for the sodiation and desodiation processes, respectively, indicating that the ionic conductivity of the material was

mechanochemically improved. Electronic and kinetic enhancements were also observed by CV and EIS measurements, with R_{ct} values three times smaller for NVPF-bm. Additionally, the diffusion lengths were estimated by combining the GITT results and EIS fitting. NVPF-bm presented values of 2.1 and 0.3 μm compared to 8.1 and 12 μm for NVPF for the charge and discharge processes, respectively. Hence, this study shows that mechanochemistry is a valuable solvent-free alternative for improving the electrochemical storage properties of NVPF-based positive electrodes for sodium-ion batteries.

Author contributions

William G. Morais: conceptualization, investigation, methodology, formal analysis, writing – original draft. Eduardo C Melo: investigation, formal analysis. Roberto R. Torresi: conceptualization, supervision, resources, writing – review, editing.

Conflicts of interest

The authors declare that there are no competing financial interests.

Acknowledgements

This work is supported by CNPq, CAPES and FAPESP (2015/26308-7 and 2021/00675-4). WGM wishes to thank FAPESP fellowship 2018/23072-0. Additionally, we would like to thank Gabrielle Cerqueira for the SEM images and Dra Susana Chauque for the XRD measurements.

References

1 R. Leithoff, A. Fröhlich and K. Dröder, Investigation of the Influence of Deposition Accuracy of Electrodes on the Electrochemical Properties of Lithium-Ion Batteries, *Energy Technol.*, 2020, **8**, 1900129.

2 V. L. Martins, H. R. Neves, I. E. Monje, M. M. Leite, P. F. M. DE Oliveira, R. M. Antoniassi, S. Chauque, W. G. Morais, E. C. Melo, T. T. Obana, B. L. Souza and R. M. Torresi, An Overview on the Development of Electrochemical Capacitors and Batteries - part II., *An. Acad. Bras. Cienc.*, 2020, **92**, e20200800.

3 P. K. Dutta, Y. Myung, R. Kulangaramadom Venkiteswaran, L. Mehdi, N. Browning, P. Banerjee and S. Mitra, Mechanism of Na-Ion Storage in BiOCl Anode and the Sodium-Ion Battery Formation, *J. Phys. Chem. C*, 2019, **123**, 11500–11507.

4 L. Yang, Y. Sun and P. Adelhelm, Electrochemical Properties of Layered Na x Ni x/2Mn1−x/2O2 $(0.5 \leq x \leq 1.1)$ with P3 Structure as Cathode for Sodium-Ion Batteries, *Energy Technol.*, 2022, **10**, 2101121.

5 K. M. Abraham, How Comparable Are Sodium-Ion Batteries to Lithium-Ion Counterparts?, *ACS Energy Lett.*, 2020, **5**, 3544–3547.

6 V. Nguyen, Y. Liu, Y. Li, S. A. Hakim, X. Yang and W. Chen, Synthesis and Electrochemical Performance of Fe2(MoO4)3/Carbon Nanotubes Nanocomposite Cathode Material for Sodium-Ion Battery, *ECS J. Solid State Sci. Technol.*, 2015, **4**, M25–M29.

7 M. S. Chae, Y. Elias and D. Aurbach, Tunnel-Type Sodium Manganese Oxide Cathodes for Sodium-Ion Batteries, *ChemElectroChem*, 2021, **8**, 798–811.

8 P. Desai, J. Forero-Saboya, V. Meunier, G. Rousse, M. Deschamps, A. M. Abakumov, J. M. Tarascon and S. Mariyappan, Mastering the synergy between Na3V2(PO4)2F3 electrode and electrolyte: A must for Na-ion cells, *Energy Storage Mater.*, 2023, **57**, 102–117.

9 H. Li, H. Chen, X. Shen, X. Liu, Y. Fang, F. Zhong, X. Ai, H. Yang and Y. Cao, High-Voltage and Intrinsically Safe Sodium Metal Batteries Enabled by Nonflammable Fluorinated Phosphate Electrolytes, *ACS Appl. Mater. Interfaces*, 2022, **14**, 43387–43396.

10 L. Xiao, F. Ji, J. Zhang, X. Chen and Y. Fang, Doping Regulation in Polyanionic Compounds for Advanced Sodium-Ion Batteries, *Small*, 2023, **19**, 2205732.

11 W. G. Morais, M. M. Leite and R. M. Torresi, Titanium- and niobium-doped fluorophosphates as positive electrodes for sodium-ion batteries, *J. Electroanal. Chem.*, 2021, **897**, 115595.

12 P. Du, K. Mi, F. Hu, X. Jiang, D. Wang and X. Zheng, Hierarchical hollow microspheres Na3V2(PO4)2F3C@rGO as high-performance cathode materials for sodium ion batteries, *New J. Chem.*, 2020, **44**, 12985–12992.

13 T. Lu, X. Yu, X. Li, J. Qi, S. Huang, Z. Man and H. Zhuo, Zwitterionic polymer-derived nitrogen and sulfur co-doped carbon-coated Na3V2(PO4)2F3 as a cathode material for sodium ion battery energy storage, *New J. Chem.*, 2021, **45**, 19391–19401.

14 Y. Lai, H. Xie, P. Li, B. Li, A. Zhao, L. Luo, Z. Jiang, Y. Fang, S. Chen, X. Ai, D. Xia and Y. Cao, Ion-Migration Mechanism: An Overall Understanding of Anionic Redox Activity in Metal Oxide Cathodes of Li/Na-Ion Batteries, *Adv. Mater.*, 2022, **34**, 2206039.

15 P. F. M. de Oliveira, R. M. Torresi, F. Emmerling and P. H. C. Camargo, Challenges and opportunities in the bottom-up mechanochemical synthesis of noble metal nanoparticles, *J. Mater. Chem. A*, 2020, **8**, 16114–16141.

16 B. L. Souza, S. Chauque, P. F. M. de Oliveira, F. F. Emmerling and R. M. Torresi, Mechanochemical optimization of ZIF-8/Carbon/S8 composites for lithium-sulfur batteries positive electrodes, *J. Electroanal. Chem.*, 2021, **896**, 115459.

17 A. Kiani, E. Lamberti, G. Viscusi, P. Giudicianni, C. M. Grottola, R. Ragucci, G. Gorrasi and M. R. Acocella, Eco-friendly one-shot approach for producing a functionalized nano-torrefied biomass: a new application of ball milling technology, *Mater. Adv.*, 2023, **5**, 695–704.

18 N. Muralidharan, C. N. Brock, A. P. Cohn, D. Schauben, R. E. Carter, L. Oakes, D. G. Walker and C. L. Pint, Tunable Mechanochemistry of Lithium Battery Electrodes, *ACS Nano*, 2017, **11**, 6243–6251.

19 S. Chauque, F. Y. Oliva, A. Visintin, D. Barraco, E. P. M. Leiva and O. R. Cámara, Lithium titanate as anode material for lithium ion batteries: Synthesis, post-treatment and its electrochemical response, *J. Electroanal. Chem.*, 2017, **799**, 142–155.

20 B. Zazoum, Evaluation and Optimization of Dielectric Properties of PVDF/BaTiO3 Nanocomposites Film for Energy Storage and Sensors, *ECS J. Solid State Sci. Technol.*, 2020, **9**, 115005.

21 M. Wang, X. Huang, H. Wang, T. Zhou, H. Xie and Y. Ren, Synthesis and electrochemical performances of Na3V2(PO4)2F3/C composites as cathode materials for sodium ion batteries, *RSC Adv.*, 2019, **9**, 30628–30636.

22 J. Cheng, Y. Chen, S. Sun, Z. Tian, Y. Linghu, Z. Tian, C. Wang, Z. He and L. Guo, Na3V2(PO4)3/C·Na3V2(PO4)2F3/C@rGO blended cathode material with elevated energy density for sodium ion batteries, *Ceram. Int.*, 2021, **47**, 18065–18074.

23 W. Massa, O. V. Yakubovich and O. V. Dimitrova, Crystal structure of a new sodium vanadyl(IV) fluoride phosphate Na3{V2O2F[PO4]2}, *Solid State Sci.*, 2002, **4**, 495–501.

24 W. Zhu, K. Liang and Y. Ren, Modification of the morphology of Na3V2(PO4)2F3 as cathode material for sodium-ion batteries by polyvinylpyrrolidone, *Ceram. Int.*, 2021, **47**, 17192–17201.

25 X. Shen, Q. Zhou, M. Han, X. Qi, B. Li, Q. Zhang, J. Zhao, C. Yang, H. Liu and Y.-S. Hu, Rapid mechanochemical synthesis of polyanionic cathode with improved electrochemical performance for Na-ion batteries, *Nat. Commun.*, 2021, **12**, 2848.

26 C. Ma, T. Xu, C. Yan, J. Xu, D. Kong, Z. Zhang, W. Shen, Y. Shi, C. Ke, X. Li and Y. Wang, Mechanism investigation of high performance Na3V2(PO4)2O2F/reduced graphene oxide cathode for sodium-ion batteries, *J. Power Sources*, 2021, **482**, 228906.

27 N. Sharma, P. Serras, V. Palomares, H. E. A. Brand, J. Alonso, P. Kubiak, M. L. Fdez-Gubieda and T. Rojo, Sodium Distribution and Reaction Mechanisms of a Na 3 V 2 O 2 (PO 4) 2 F Electrode during Use in a Sodium-Ion Battery, *Chem. Mater.*, 2014, **26**, 3391–3402.

28 J. Xu, J. Chen, L. Tao, Z. Tian, S. Zhou, N. Zhao and C.-P. Wong, Investigation of Na3V2(PO4)2O2F as a sodium ion battery cathode material: Influences of morphology and voltage window, *Nano Energy*, 2019, **60**, 510–519.

29 W. Weppner and R. A. Huggins, Electrochemical Methods for Determining Kinetic Properties of Solids, *Annu. Rev. Mater. Sci.*, 1978, **8**, 269–311.

30 H. Yang, H. J. Bang and J. Prakash, Evaluation of Electrochemical Interface Area and Lithium Diffusion Coefficient for a Composite Graphite Anode, *J. Electrochem. Soc.*, 2004, **151**, A1247.

31 D. W. Dees, S. Kawauchi, D. P. Abraham and J. Prakash, Analysis of the Galvanostatic Intermittent Titration Technique (GITT) as applied to a lithium-ion porous electrode, *J. Power Sources*, 2009, **189**, 263–268.

32 M. C. H. McKubre and D. D. Macdonald, *Impedance Spectroscopy*, 2005, pp. 129–204.

33 M. E. Orazem and B. Tribollet, *Electrochemical Impedance Spectroscopy*, 2008, pp. 333–351.

34 X. Fan, L. Chen, O. Borodin, X. Ji, J. Chen, S. Hou, T. Deng, J. Zheng, C. Yang, S.-C. Liou, K. Amine, K. Xu and C. Wang, Non-flammable electrolyte enables Li-metal batteries with aggressive cathode chemistries, *Nat. Nanotechnol.*, 2018, **13**, 715–722.

35 S. Jiao, X. Ren, R. Cao, M. H. Engelhard, Y. Liu, D. Hu, D. Mei, J. Zheng, W. Zhao, Q. Li, N. Liu, B. D. Adams, C. Ma, J. Liu, J.-G. Zhang and W. Xu, Stable cycling of high-voltage lithium metal batteries in ether electrolytes, *Nat. Energy*, 2018, **3**, 739–746.

36 M. Zarrabeitia, T. Rojo, S. Passerini and M. Á. Muñoz-Márquez, Influence of the Current Density on the Interfacial Reactivity of Layered Oxide Cathodes for Sodium-Ion Batteries, *Energy Technol.*, 2022, **10**, 2200071.

37 T. Q. Nguyen and C. Breitkopf, Determination of Diffusion Coefficients Using Impedance Spectroscopy Data, *J. Electrochem. Soc.*, 2018, **165**, E826–E831.